KSME

Springer

Journal of Mechanical Science and Technology 37 (12) 2023

Original Article
DOI 10.1007/s12206-023-2407-0

Keywords:
· Auxetic metamaterial
· Re-entrant lattice structure
· Finite element analysis
· Additive manufacturing
· Negative Poisson's ratio

Correspondence to:
Keun Park
kpark@seoultech.ac.kr

Citation:
Choi, H.-G., Park, K. (2023). Deformation behavior of re-entrant auxetic metamaterials considering shape transformation effects. Journal of Mechanical Science and Technology 37 (12) (2023) 6143~6151.
http://doi.org/10.1007/s12206-023-2407-0

Received August 1st, 2023
Revised September 10th, 2023
Accepted September 10th, 2023

† This paper was presented at ICMDT2023, Ramada Plaza Hotel, Jeju, Korea, March 8-11, 2023. Recommended by Guest Editor Hyung Wook Park

Deformation behavior of re-entrant auxetic metamaterials considering shape transformation effects

Hong-Gap Choi and Keun Park

Department of Mechanical System Design Engineering, Seoul National University of Science and Technology, Seoul 01811, Korea

Abstract A re-entrant hexagonal structure is the most popularly-used auxetic metamaterial providing unique deformation behavior with a negative Poisson's ratio. In the re-entrant auxetic structure, the Poisson's ratio varies depending on the design of the re-entrant shape and the order of deformation. In this study, the deformation behavior of re-entrant auxetic structures was investigated through experimental and numerical analyses, with a variation of the re-entrant angle. The experimental results showed that the Poisson's ratio increased as the re-entrant angle decreased, and the auxetic property was maintained only while a re-entrant cell remained in a concave shape. Finite element analyses (FEAs) were also conducted to investigate the deformation behavior of the re-entrant structures, using 1D-beam and 2D-continuum elements. Compared to the experimental findings, the 2D-FEA showed similar results both in the concave and convex deformation regimes whereas the 1D-FEA showed a reliable prediction only in the concave regime. Additionally, consideration of the cell curvature in the 2D-FEA provided better simulation accuracy by appropriately describing the transformation from the concave to convex regimes. The relevant Poisson's ratio data were then statistically analyzed to obtain a bilinear regression equation as a function of the axial strain and re-entrant angle, which provides insights into the deformation behavior of re-entrant structures.

1. Introduction

Metamaterials are artificially designed micro-architectures that possess unique and exceptional physical properties. The initial investigations into metamaterials have primarily concentrated on the changes in optical or electromagnetic characteristics, such as a negative refractive index in a transparent cloak [1, 2]. The idea of metamaterials was expanded upon to achieve exceptional mechanical properties, yielding materials referred to as mechanical metamaterials [3].

Mechanical metamaterials exhibit unusual mechanical properties by means of microscale architectures: auxetic metamaterials characterized by a negative Poisson's ratio [4, 5], pentamode metamaterials characterized by an extremely high bulk modulus compared to its shear modulus [6], and 3D chiral metamaterials characterized by compression-twist behaviors [7]. These mechanical metamaterials have complex micro-architectured geometries and thus cannot be fabricated by the traditional manufacturing processes. In the past decade, additive manufacturing (AM) has been used to fabricate various mechanical metamaterials with extreme mechanical properties [8]: ultralight and ultrastiff structures [9], an extremely high bulk to shear modulus [10], and extreme compliance differences [11]. Whereas these mechanical metamaterials realized unique structural properties, microscale architectures have also been studied to derive unique thermal properties such as negative thermal expansion [12], adjustable heat flux [13], and achievement of the two conflicting objectives of thermal resistivity and cooling capabilities [14].

The objective of the present study is to investigate the deformation behavior of auxetic

metamaterials, focusing on their capability of a tunable Poisson's ratio. More specifically, deformation behaviors of re-entrant auxetic structures are investigated numerically and experimentally. The re-entrant structure is the most popularly-used auxetic structure [15], and has advantages in terms of enhanced impact resistance [16] and energy absorption characteristics [17] besides the auxetic property itself. The deformation behavior of the re-entrant structure was numerically investigated using a finite element analysis (FEA), mostly using 1D finite element (FE) models for computational efficiency [18, 19]. Although a full-3D FEA was also performed using 3D continuum elements, discretization of microscale ligaments requires a high computational load [20], and hence a simplified FE model such as computational homogenization is required [21].

In this study, numerical analyses for 2D re-entrant auxetic structures were conducted to investigate deformation behavior with a variation of the re-entrant angle. Two types of FEAs using 1D-beam and 2D-continuum elements were used in discretizing a number of periodic re-entrant cells. In the case of the 2D-FEA, two FE models were used depending on whether the natural curvature is considered at every junction. Three FEA cases were then conducted and compared with experiments in terms of the lateral deformation and the relevant Poisson's ratio. In particular, the computational accuracy was discussed in terms of describing the shape transformation from the concave to convex regimes. The relevant Poisson's ratio data were then statistically analyzed to obtain a bilinear regression equation as a function of the axial strain and re-entrant angle.

2. Deformation behavior of re-entrant auxetic structures

2.1 Design of re-entrant auxetic structure

Auxetic metamaterials are defined by a negative Poisson's ratio, which is generally known to have a positive value in typical materials [22]. The most popularly used auxetic structure is the re-entrant hexagonal structure. Fig. 1(a) presents a schematic illustration of a re-entrant auxetic structure, the deformation of which is dominated by the re-alignment of the cell hinges [4]. Accordingly, its stretching deformation along the vertical direction induces horizontal expansion, and the resulting apparent Poisson's ratio (ν^*) becomes negative according to the definition of Eq. (1):

$$\nu^* = -\frac{\varepsilon_y^*}{\varepsilon_x^*} \tag{1}$$

where ε_x^* and ε_y^* denote the apparent strain components along the horizontal (x) and vertical (y) directions, respectively.

Fig. 1(b) shows a unit cell of the re-entrant structure with a cell size of l. Here, the re-entrant angle (θ) was set to a design parameter, and four control points (P_1 to P_4) were set to the midpoint of each ligament. These control points were fixed at the l/4 locations from the corner points of the unit cell, and θ was varied to generate different re-entrant shapes. The relevant lengths of an inclined ligament (a) and a vertical ligament (b) were then determined depending on θ, as in the following equations.

$$a = \frac{l}{2\cos\theta} \tag{2}$$

$$b = \frac{l}{2}(1+\tan\theta)\,. \tag{3}$$

Fig. 1(c) shows the change of the re-entrant unit cells according to the variations of θ, from 0 to 30° with an increment of

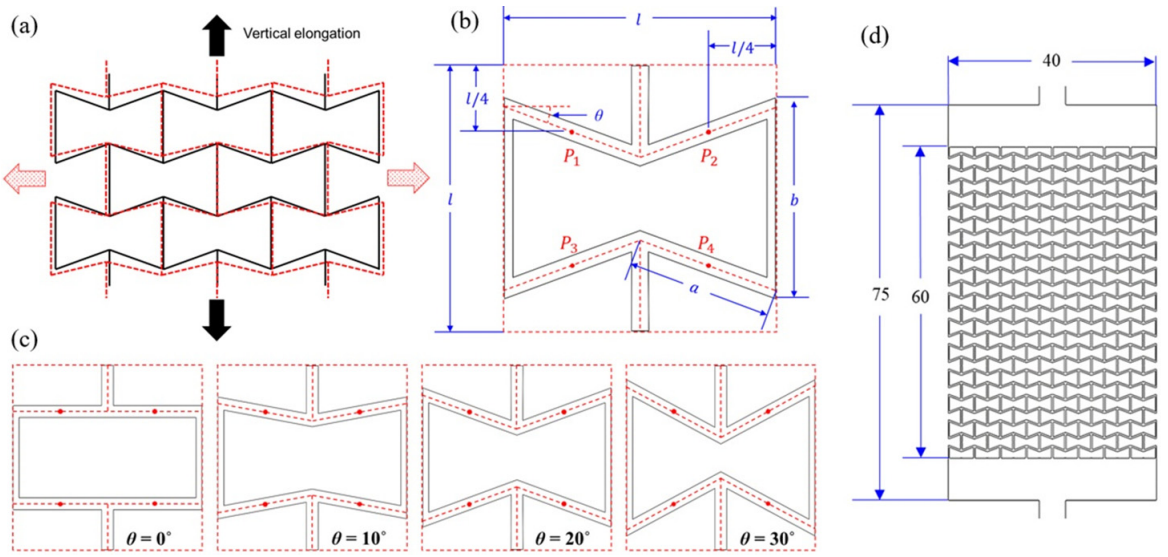

Fig. 1. Definition of a re-entrant auxetic structure: (a) deformation behavior of a re-entrant structure; (b) unit cell with design parameters; (c) unit cells with different re-entrant angles; (d) design of a tensile specimen (θ = 20°).

10°. In all designs, the cell size (l) and ligament width (w) were set to 5.0 and 0.3 mm, respectively. Fig. 1(d) shows the re-entrant structure for a tensile test specimen including 8 × 12 re-entrant cells with a 20° re-entrant angle. The outer dimensions of this specimen are 40 × 75 × 10 mm including additional solid regions for proper gripping.

2.2 Additive manufacturing

The designed tensile specimens were additively manufactured using a DLP 3D printer (IMD, Carima Inc., Korea). This printer uses a UV lamp (405 nm wavelength) at a power of 500 mW and a high-definition digital micromirror device chip (1920 × 1080 pixels). A photo-curable polyurethane resin (CUTK05B, Carima Inc., Korea) was used as a printing material, which is composed of diluted urethane acrylate, photoinitiator (Irgacure 819), and black color pigment. In the resin state, its density and viscosity are 1.10 g/cm^3 and 365 cps, respectively. After photocuring, this photopolymer has a 1.2 GPa elastic modulus and 54.8 MPa tensile strength [23]. The layer thickness, irradiation time per layer, and UV irradiation energy density were set to 50 μm, 3.1 s, and 6.4 mW/cm^2, respectively.

To remove the residual photopolymer resin after AM, additively manufactured specimens were rinsed with 99.5 % isopropyl alcohol in an ultrasonic cleaning machine (SD-250H, Mujigae Co. Ltd., Korea). These specimens were then additionally cured using a UV-curing device (CL300, Carima Inc., Korea), the power and curing time of which were set to 300 W and 15 s, respectively.

Fig. 2(a) shows the additively manufactured tensile specimens with a 20° re-entrant angle. Fig. 2(b) is a microscopic image of the specimen, showing that microscale re-entrant cells were printed without defects. It was observed that natural curvatures were formed at the joints of the re-entrant ligaments. These natural curvatures originated from the curing of the residual photopolymer resin at the joint regions. The radii of the curvatures at the concave (R_1) and convex (R_2) edges were measured to be 0.153 and 0.803 mm, respectively, and the relevant effect on the accuracy of the FE analysis will be considered in Sec. 3.

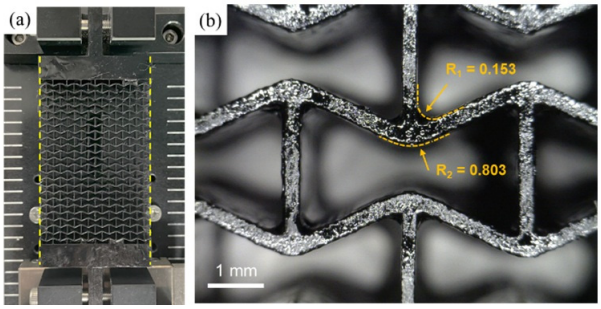

Fig. 2. Additively manufactured auxetic structures (θ = 20°): (a) photograph of a tensile specimen; (b) magnified image with the radius dimensions (unit: mm).

2.3 Tensile deformation behavior

Tensile tests were conducted to investigate the deformation behaviors of the re-entrant specimens. Fig. 3(a) shows the experimental setup for the tensile test. A tensile specimen containing a number of re-entrant cells was installed on the grippers of the tensile-test equipment. The test equipment then elongated the specimen with a stepwise stroke of 2 mm. A 3D scanner (C500, Solutionix Corp., Korea) was installed on top of the equipment and scanned the deformed shape of the specimen at every step. Fig. 3(b) shows a photograph of a tensile specimen under vertical elongation (θ = 30°). It can be seen that the specimen laterally elongated as the re-entrant cells were expanded both in the vertical and horizontal directions.

Fig. 3(c) plots the amounts of lateral deformation with an increase in axial deformation. It can be seen that the lateral deformation decreases to have negative values when the re-entrant angle is zero (i.e. a rectangular unit cell without a re-

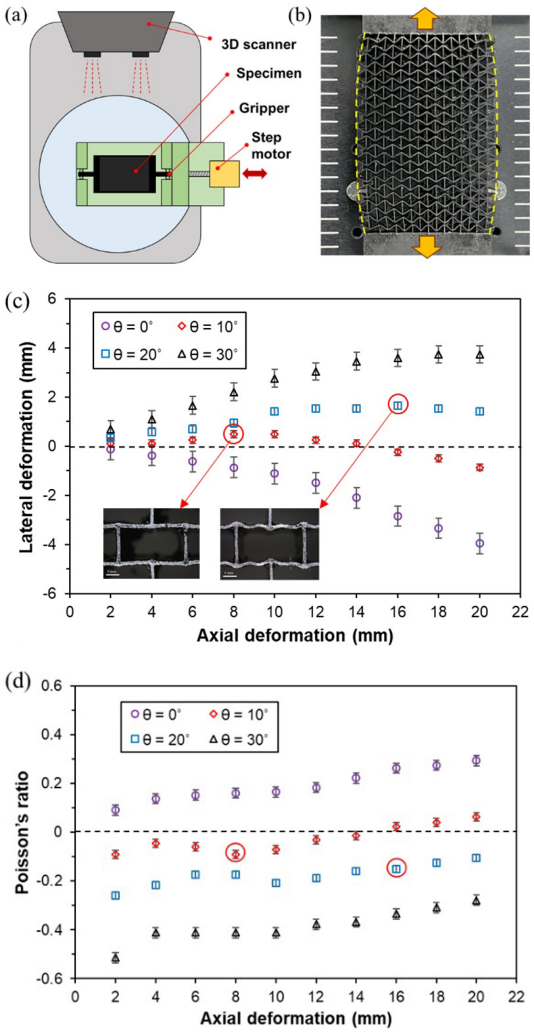

Fig. 3. Tensile experiment results for different re-entrant angles: (a) experimental setup; (b) deformed shape of a re-entrant specimen (θ = 20°); (c) lateral deformation; (d) the resulting Poisson's ratio.

entrant feature). This indicates that this specimen did not show auxetic behavior because a rectangular cell cannot be regarded as a re-entrant structure.

On the contrary, the other three cases with positive re-entrant angles show auxetic behaviors with positive lateral deformations. However, they show different deformation behaviors according to the size of the re-entrant angle. First, the amount of lateral deformation increased as the re-entrant angle increased. Second, the 10 and 20° cases showed local maximum values, as marked in Fig. 3(c), and then decreased after these points. These trends are different from the 30° angle case, which shows a monotonic increase until the 20 mm axial deformation. To investigate this difference, deformed shapes at the critical points (i.e., 10 mm axial deformation for the 10° angle case and 16 mm axial deformation for the 20° angle case) are included in Fig. 3(c). It is notable that both cases show nearly rectangular shapes at the critical location, which indicates that the auxetic behavior of the re-entrant structure is valid as long as the re-entrant cells maintain the concave shape.

Fig. 3(d) shows the corresponding changes in the Poisson's ratio. The 0° angle case shows positive values in the entire deformation range, whereas the Poisson's ratios remain negative when the re-entrant angle is 20 and 30°. When the re-entrant angle is 10°, on the contrary, the Poisson's ratio transitions from negative to positive as the axial displacement increases. These results indicate that the re-entrant angle must be designed to be sufficiently high to ensure auxetic behavior: higher than 20° in the current deformation range.

3. Finite element analysis of re-entrant auxetic structures

FE analyses (FEAs) were conducted using ANSYS Workbench (ANSYS Inc., USA) to investigate the deformation behaviors of the re-entrant structures. A quarter model of each tensile specimen was taken into account by considering the geometric symmetry. As a boundary condition, a vertical displacement of 20 mm was imposed, with an increment of 0.2 mm. Two types of FE elements, 1D-beam and 2D-continuum elements, were used in the simulations, and the relevant results are discussed in the following subsections.

3.1 FE analysis using 1D-beam elements

For computational efficiency, the re-entrant auxetic structures were discretized by a number of 1D-beam elements. The displacement field of a beam element (v) is described by the following equation:

$$v(u) = S_1(u)v_1 + S_2(u)\theta_1 + S_3(u)v_2 + S_4(u)\theta_2 \tag{4}$$

where v_i and θ_i denote the nodal displacement and rotation for the i-th node, respectively. The functions $S_i(u)$ are the corresponding Hermite blending functions, expressed as the following cubic form of a parameter u ($0 \leq u \leq 1$).

Table 1. Summarization of 1D FE models with different re-entrant angles.

Re-entrant angles (°)	0	10	20	30
No. of nodes	6657	7723	8373	8607
No. of elements	3429	3962	4287	4404

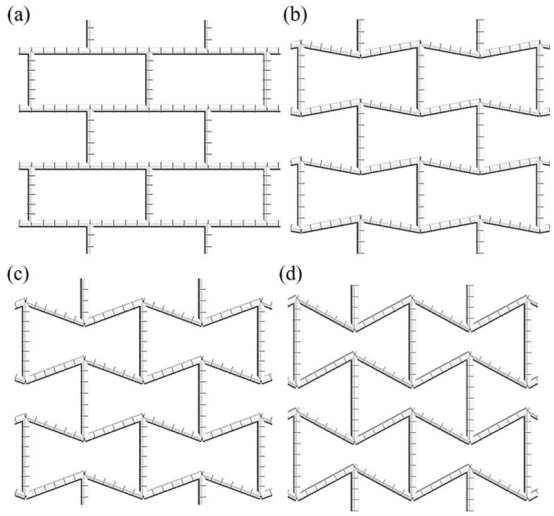

Fig. 4. FE models using 1D-beam elements for various re-entrant angles: (a) 0°; (b) 10°; (c) 20°; (d) 30°.

$$S_1(u) = 1 - 3u^2 + 2u^3, \tag{5a}$$

$$S_2(u) = 3u^2 - 2u^3, \tag{5b}$$

$$S_3(u) = u - 2u^2 + u^3, \tag{5c}$$

$$S_4(u) = -u^2 + u^3. \tag{5d}$$

Figs. 4(a)-(d) show the discretized FE models for different re-entrant angles, wherein 1D mesh structures in four unit cells (i.e., 2×2 cells) are displayed for visibility. The mesh size was set to 0.5 mm, and the resulting numbers of the nodes and elements for each FE model are summarized in Table 1. For convenience, this 1D-FEA is referred to as case 1, distinguished from the 2D-FEAs to be introduced in the next section.

Fig. 5(a) shows the variations of lateral deformations with increased axial deformation. Overall, the simulation results show similar trends to the experimental results; the amount of lateral deformation increased as the re-entrant angle increased. However, the degree of similarity between the simulation and experiment showed a different tendency depending on the re-entrant angle. First, the simulation and experimental results tend to be almost identical when the re-entrant angle is 30°. For the cases of the 10° and 20° re-entrant angles, the differences between the simulation and experimental results increase with an increase in axial deformation. More specifically, these differences increase significantly from the marked critical points (i.e., 10 mm for the 10° angle case and 16 mm for the 20° angle case).

Fig. 5(b) shows the obtained Poisson's ratios compared to the experimental findings, showing linearly increasing trends with an

Table 2. Comparison of the ranges of Poisson's ratio (1D-FE simulation).

Re-entrant angle (°)		0	10	20	30
Simulation	2 mm	0.0171	-0.1627	-0.3454	-0.5184
	10 mm	0.0888	-0.0912	-0.2645	-0.4304
	20 mm	0.1914	-0.0075	-0.1718	-0.3241
Experiment	2 mm	0.0918	-0.0897	-0.2592	-0.5147
	10 mm	0.1653	-0.0717	-0.2074	-0.4118
	20 mm	0.2938	0.0628	-0.1037	-0.2779

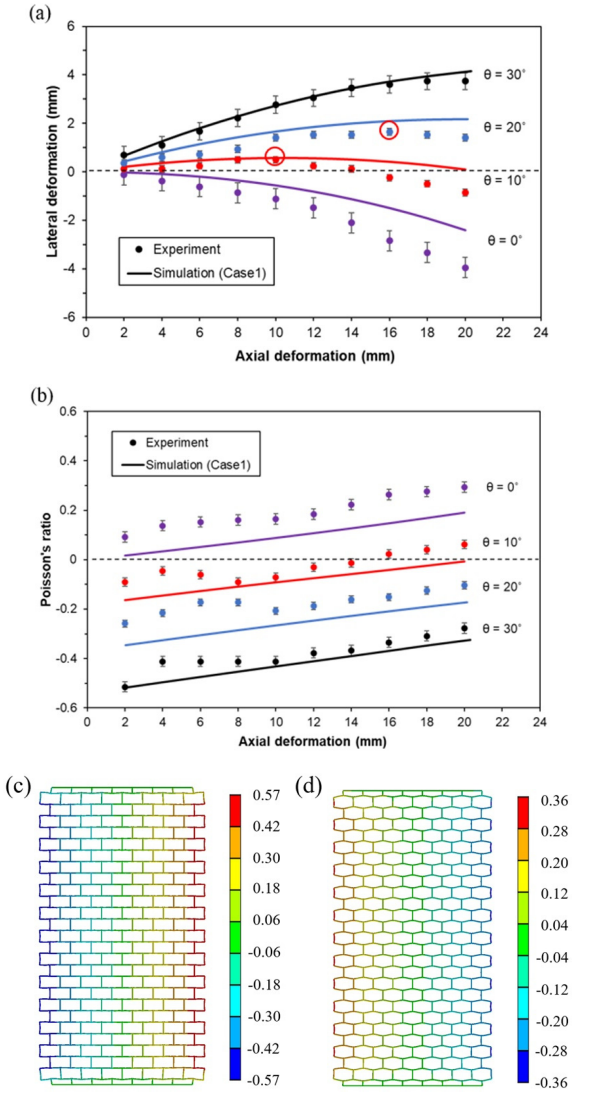

Fig. 5. FE simulation results using 1D beam elements: (a) comparison of lateral deformation; (b) comparison of Poisson's ratio; (c) deformed shape at 10 mm elongation (θ = 10°); (d) deformed shape at 10 mm elongation (θ = 0°). In (c) and (d), color contours denote the lateral displacements (unit: mm).

increase in axial deformation. The resulting Poisson's ratios are compared in Table 2, in a range of axial deformations between 2 and 20 mm. The Poisson's ratio showed positive values in the 0° angle case, with a monotonic increasing trend from 0.0171 to 1.914. Other cases with positive re-entrant angles show negative Poisson's ratios, showing a minimum value of -0.5184 when the 30° angle case was elongated by 2 mm. These simulation results are slightly lower than the experimental findings. The difference between the simulation and experiment is the smallest when the re-entrant angle is 30°, whereas the difference is the largest when the re-entrant angle is 0°.

Fig. 5(c) is the deformed shape of the 10° angle specimen after 10 mm elongation, which corresponds to the critical deformation. Here, the color contour indicates the amount of lateral deformation. The left side of the specimen shows negative deformation while the right side shows positive deformation, indicating that the specimen undergoes lateral expansion. Accordingly, this specimen exhibits auxetic behavior with a negative Poisson's ratio. It is also notable that the re-entrant cells are transformed from concave shapes into nearly rectangular shapes at this stage, showing a similar result to that of the experiment.

Fig. 5(d) presents the deformed shape of the 0° angle specimen after 10 mm elongation, showing that a rectangular cell is transformed into a convex honeycomb shape. Furthermore, the left side shows positive deformation while the right side shows negative deformation, and the resulting Poisson's ratio is positive in this regime. Considering that the simulation result shows the largest error in this case, the transition from a concave regime to a convex regime cannot be accurately predicted through the 1D-FEA.

3.2 FE analysis using 2D-continuum elements

For better prediction of deformation behaviors of re-entrant structures, a FE analysis was also conducted using 2D-continuum elements. Four-node quadrilateral elements were used for the 2D FE simulation. In this element, a position vector **P**(x, y) can be represented by linear interpolation using a natural coordinate (ξ, η) in the range of [-1, 1]:

$$x = \sum_{i=1}^{4} N_i(\xi,\eta)\, x_i \tag{6a}$$

$$y = \sum_{i=1}^{4} N_i(\xi,\eta)\, y_i \tag{6b}$$

where $N_i(\xi, \eta)$ is the isoparametric shape function for a four-node quadrilateral element, given by the following equation:

$$N_i(\xi,\eta) = \frac{1}{4}(1+\xi\xi_i)(1+\eta\eta_i)\,. \tag{7}$$

Four re-entrant tensile specimens with different re-entrant angles were then discretized using 2D quadrilateral elements. The element size was set to 0.08 mm, and the resulting mesh structures for four unit cells are shown in Figs. 6(a)-(d). This 2D FE model without consideration of the natural curvature is referred to as case 2. For further discussion of the curvature effect, the

Table 3. Summarization of 2D FE models with different re-entrant angles.

Re-entrant angles (°)		0	10	20	30
Case 2	No. of nodes	95360	104882	114751	123388
	No. of elements	76828	85576	93606	100593
Case 3	No. of nodes	108646	105393	114121	132677
	No. of elements	91848	86620	93872	109919

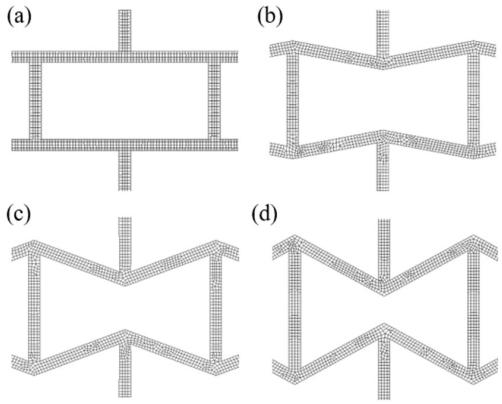

Fig. 6. FE models using 2D quadrilateral elements for various re-entrant angles (case 2): (a) 0°; (b) 10°; (c) 20°; (d) 30°.

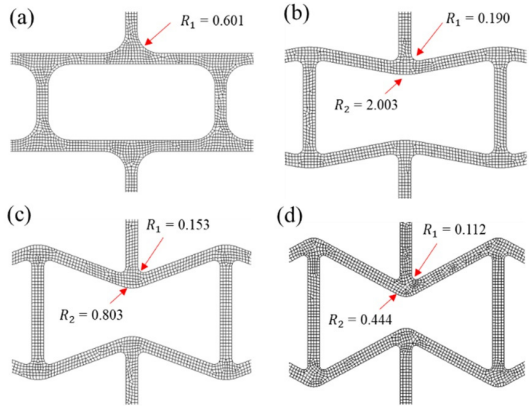

Fig. 7. FE models using 2D beam elements for various re-entrant angles (case 3, unit: mm): (a) 0°; (b) 10°; (c) 20°; (d) 30°.

2D models were modified to have curvatures at the junctions of the re-entrant cells, as mentioned in Sec. 2.2 (Fig. 2(b)).

Figs. 7(a)-(d) show the 2D mesh structures of four unit cells when the radii of curvatures (R_1 and R_2) were considered. These radius values were measured from the specimen photographs, and the average values from all junctions were calculated. This 2D FE model is referred to as case 3, and the resulting numbers of nodes and elements are listed in Table 3.

The results of the 2D-FEA without the curvature consideration (case 2) are demonstrated in Figs. 8(a) and (b). Fig. 8(a) shows the variations of lateral deformations compared to the experimental results. Overall, the simulation results show similar trends to the 1D-FEA results in Fig. 5(a); the simulation and experimental results are similar when the re-entrant angle is 30° while the zero re-entrant angle case shows the largest

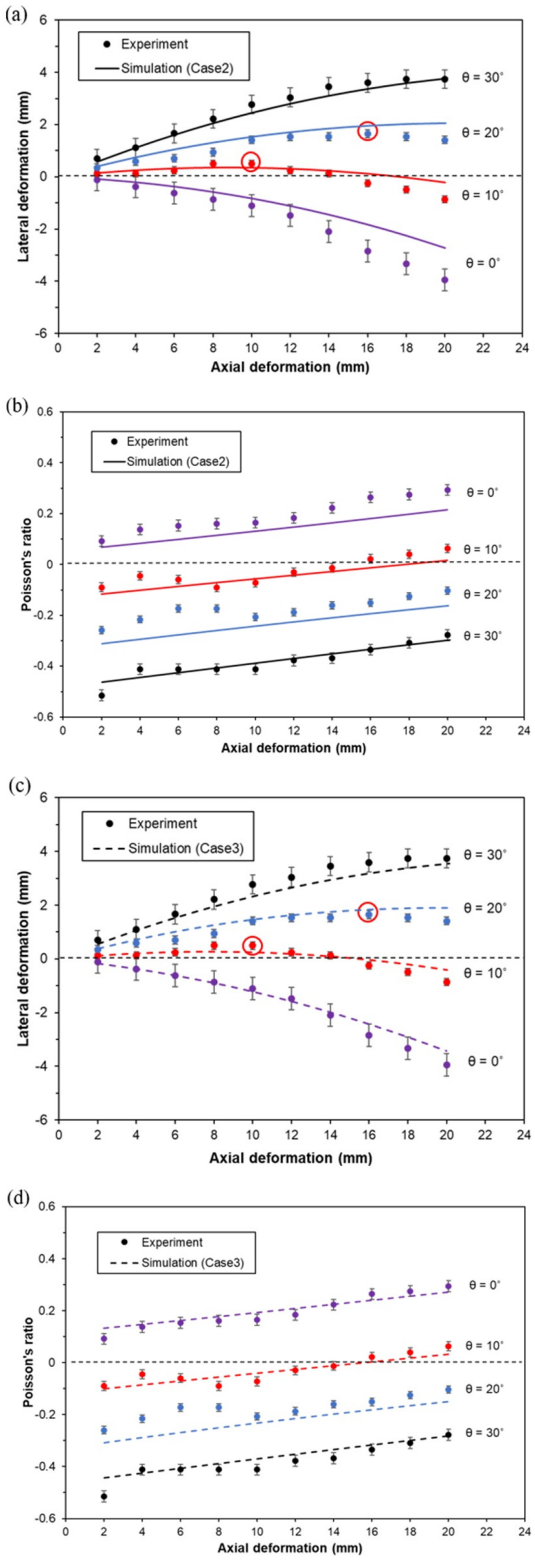

Fig. 8. FEA results using 2D-continuum elements: (a) lateral deformation (case 2); (b) Poisson's ratio (case 2); (c) lateral deformation (case 3); (d) Poisson's ratio (case 3).

difference. Fig. 8(b) compares the resulting Poisson's ratios with those of experiments, showing similar trends with the re-

sults of the 1D-FEA; the difference between the simulation and experiment is the largest when the re-entrant angle is 0°.

The results of the 2D-FEA with consideration of the curvature (case 3) are shown in Figs. 8(c) and (d). It is notable that the simulation results are similar to those of experiments even when the re-entrant angle is 0°, as exhibited in Fig. 8(c). As illustrated in Fig. 8(d), the resulting Poisson's ratios show better predictions than those of case 2 (Fig. 8(b)). These results indicate that the 2D-FEA with consideration of the curvature predicts the deformation behavior of a re-entrant auxetic structure more accurately, especially in the regime of convex deformation.

3.3 Comparison of deformation behaviors

For further discussion of the simulation accuracy, the deformed shapes of the 20° re-entrant angle case were compared in detail. Figs. 9(a)-(c) compare the deformed shapes of unit cells for three FEA cases, at 10 mm vertical elongation. Here, the lower junction regions were magnified, and the relevant deformation profiles are plotted as dotted lines. It can be seen that the deformation profiles of cases 1 and 2 are almost identical, showing that the two ligaments are connected sharply at the junctions. In contrast, case 3 shows a smooth connection at the junction owing to the consideration of the rounded geometry, and hence provides better prediction of the real deformation behaviors [24].

This difference in the deformation profile further increased when the axial elongation was increased to 18 mm, as exhibited in Fig. 10. Overall, the deformed unit cells were transformed into rectangular shapes at this stage. However, cases 1 and 2 exhibit locally concave profiles at the junctions, as shown in Figs. 10(a) and (b). These locally concave profiles prevent an appropriate transformation from the concave to convex regimes, which resulted in simulation errors of these two cases in the convex regime, as shown in Figs. 5(a) and 8(a). In contrast, case 3 shows a nearly horizontal profile with a smooth connection, thus providing a reliable prediction of the shape transformation of a re-entrant unit cell into a convex hexagonal shape.

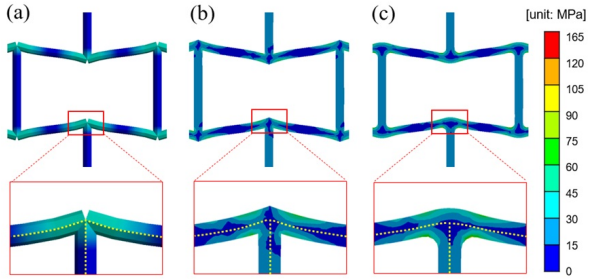

Fig. 9. Deformed shapes and stress distributions of re-entrant unit cells at 10 mm elongation (θ = 20°): (a) case 1; (b) case 2; (c) case 3.

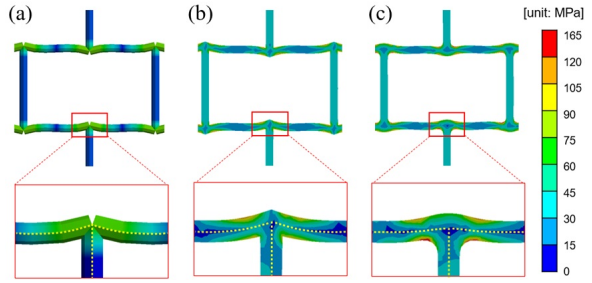

Fig. 10. Deformed shapes and stress distributions of re-entrant unit cells at 18 mm elongation (θ = 20°): (a) case 1; (b) case 2; (c) case 3.

4. Discussion

4.1 Comparison with experimental results

Fig. 11(a) compares the results of lateral deformations of various cases when the re-entrant angle is 0° because this specimen showed the largest deviations between the simulation and experimental results. It can be seen that case 3 shows the most reliable prediction with the smallest deviations whereas case 1 shows the largest deviations. Considering that the rectangular unit cells (i.e., θ = 0°) transform into convex hexagonal shapes, the deformation behavior in the convex regime could not be appropriately described by 1D-beam elements. Although the 2D-FEAs showed better predictions than the 1D-FEA in this regime, the radius of curvature at each junction must be considered to obtain better simulation accuracy [25].

Fig. 11(b) shows the lateral deformations of the 30° re-entrant angle case, where all specimens are deformed in the

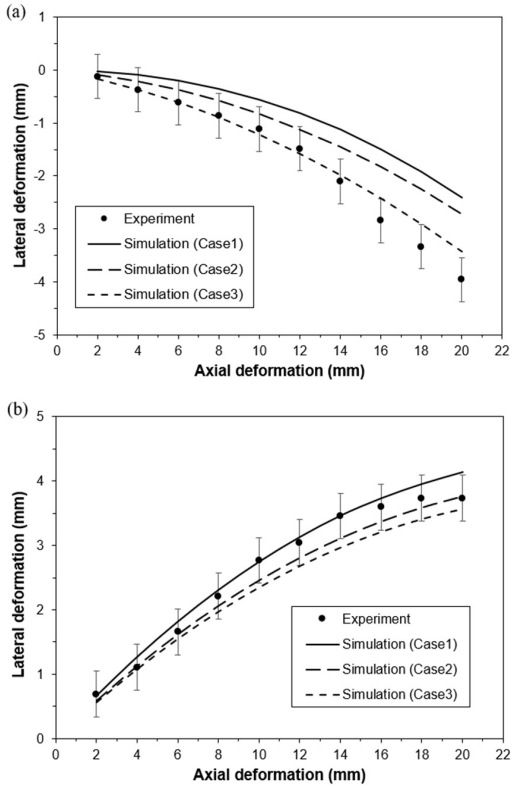

Fig. 11. Comparison of lateral deformations for different re-entrant angles: (a) θ = 0°; (b) θ = 30°.

Table 4. Comparison of the bilinear regression coefficients.

Coefficients	c_0	c_1	c_2	c_3	R^2
Case 0	0.0819	0.1866	-0.0185	0.00052	0.985
Case 1	-0.0035	0.1798	-0.0178	-0.00090	0.999
Case 2	0.0469	0.1533	-0.0179	0.00082	0.996
Case 3	0.0955	0.1490	-0.0193	0.00103	0.987

concave regime. It can be seen that the three simulation results show similar trends with those of the experiment, within the error-bar ranges. This indicates that the deformation behavior in the concave regime can be reliably predicted by the 1D-FEA because a concave unit cell remains concave without a transformation into a rectangular or a convex shape. Accordingly, the 1D-FEA is advantageous in terms of computational efficiency in the concave regime because the number of nodes of the 1D-FEA (8607) is much smaller than those of the 2D-FEAs; 123338 nodes for case 2 and 132677 nodes for case 3.

4.2 Statistical analysis

As shown in Figs. 5 and 8, Poisson's ratios of the re-entrant structures show linear relationships with the amount of axial displacement (i.e., elongation). To analyze these relationships statistically, a regression analysis was conducted to express the apparent Poisson's ratio (υ^*) as a bilinear function of the axial strain (ϵ) and re-entrant angle (θ):

$$\upsilon^*(\epsilon,\theta) = c_0 + c_1\epsilon + c_2\theta + c_3\epsilon\theta \tag{8}$$

where c_0 to c_3 are coefficients of the bilinear regression equation.

Through the regression, the regression coefficients for all cases were calculated as listed in Table 4. For the experimental results (case 0), the coefficient of determination (R^2 value) for this regression equation was calculated to be 98.5 %, showing a high correlation. However, the FEA results show different regression coefficients as compared in Table 4. Among the three simulation cases, case 3 shows the most similar coefficients to those of case 0. Moreover, the corresponding R^2 value was 98.7 % whereas those of the other simulations (i.e., cases 1 and 2) are nearly 1. This slightly low R^2 value of case 3 indicates that a slight nonlinearity exists in the deformation behavior, which is similar to the experimental findings.

5. Conclusions

In this study, the deformation behaviors of re-entrant auxetic structures were investigated through experimental and numerical analyses, with variations of the re-entrant angle. For the experiment, the designed re-entrant structures were additively manufactured using a DLP 3D printer, and tensile tests were performed to measure the lateral deformations. The resulting Poisson's ratios showed negative values when the concave re-entrant cells maintained concave shapes, and their magnitudes increased as the re-entrant angle increased; the lowest Poisson's ratio in this concave regime (i.e., the highest magnitude) was -0.5147 when the re-entrant angle was 30°, which is significantly outside of the range of the usual Poisson's ratio (between 0 and 0.5). In contrast, the Poisson's ratio showed positive values (0.0918 - 0.2938) when the re-entrant angle was 0° because the rectangular unit cells transformed into convex hexagonal shapes in this regime.

Numerical analyses were conducted to investigate these deformation behaviors using three FEA models: 1D-FEA (case 1) and 2D-FEAs without and with consideration of the natural curvature (cases 2 and 3). The FEA results of all cases showed similar trends with the experimental results in the concave regime. In the convex regime, however, cases 1 and 2 showed large deviations from the experimental results, while case 3 provided the most reliable prediction. Therefore, the natural curvature at each junction should be considered to improve simulation accuracy, by appropriately describing the transformation from the concave to convex regimes. Meanwhile, the 1D-FEA is still advantageous in the concave regime because it provides allowable accuracy with significantly reduced computational loads.

Furthermore, regression analyses showed that the Poisson's ratio could be expressed as a bilinear function of the axial strain and re-entrant angle with a high correlation, in which case 3 showed the most reliable prediction with the most similar coefficients to those of the experiments. These findings provide insights into the deformation behavior of re-entrant auxetic structures, which can be applied to the design of various re-entrant structures by providing tunable Poisson's ratio. It is anticipated that further studies will be able to extend the use of re-entrant structures to the design of functional components, in which the developed FEA schemes can be usefully applied.

Acknowledgments

This research was financially supported the National Research Foundation of Korea (NRF) grant funded by the Ministry of Science and ICT, Republic of Korea (Grant number: 2022 R1A4A1032030).

Nomenclature

ν^* : Apparent Poisson's ratio
ε^* : Apparent strain
θ : Re-entrant angle
a : Inclined ligament length
b : Vertical ligament length
l : Cell size
w : Ligament width
R_1 : Concave edge round
R_2 : Convex edge round
$\boldsymbol{P}(x,y)$: Position vector
c_n : Coefficients of the bilinear regression equation

References

[1] D. R. Smith, J. B. Pendry and M. C. Wiltshire, Metamaterials and negative refractive index, *Science*, 305 (5685) (2004) 788-792.

[2] J. Valentine, S. Zhang, T. Zentgraf, E. Ulin-Avila, D. A. Genov, G. Bartal and X. Zhang, Three-dimensional optical metamaterial with a negative refractive index, *Nature*, 455 (7211) (2008) 376-379.

[3] S. Pyo and K. Park, Mechanical metamaterials for Sensor and actuator applications, *International Journal of Precision Engineering and Manufacturing-Green Technology* (2023) https://doi.org/10.1007/s40684-023-00549-w.

[4] H. M. Kolken and A. A. Zadpoor, Auxetic mechanical metamaterials, *RSC Advances*, 7 (9) (2017) 5111-5129.

[5] X. Ren, R. Das, P. Tran, T. D. Ngo and Y. M. Xie, Auxetic metamaterials and structures: a review, *Smart Materials and Structures*, 27 (2) (2018) 023001.

[6] M. Kadic, T. Bückmann, R. Schittny, P. Gumbsch and M. Wegener, Pentamode metamaterials with independently tailored bulk modulus and mass density, *Physical Review Applied*, 2 (5) (2014) 054007.

[7] W. Wu, W. Hu, G. Qian, H. Liao, X. Xu and F. Berto, Mechanical design and multifunctional applications of chiral mechanical metamaterials: a review, *Materials and Design*, 180 (2019) 107950.

[8] R. Schwaiger, R. Meza and X. Li, The extreme mechanics of micro-and nanoarchitected materials, *MRS Bulletin*, 44 (10) (2019) 758-765.

[9] X. Zheng, H. Lee, T. H. Weisgraber, M. Shusteff, J. DeOtte and E. B. Duoss, Ultralight, ultrastiff mechanical metamaterials, *Science*, 344 (6190) (2014) 1373-1377.

[10] T. Bückmann, M. Thiel, M. Kadic, R. Schittny and M. Wegener, An elasto-mechanical unfeelability cloak made of pentamode metamaterials, *Nature Communications*, 5 (1) (2014) 4130.

[11] J. H. Park and K. Park, Compressive behavior of soft lattice structures and their application to functional compliance control, *Additive Manufacturing*, 33 (2020) 101148.

[12] Q. Wang, J. A. Jackson, Q. Ge, J. B. Hopkins, C. M. Spadaccini and N. X. Fang, Lightweight mechanical metamaterials with tunable negative thermal expansion, *Physical Review Letters*, 117 (17) (2016) 175901.

[13] K. P. Vemuri, F. M. Canbazoglu and P. R. Bandaru, Guiding conductive heat flux through thermal metamaterials, *Applied Physics Letters*, 105 (19) (2014) 193904.

[14] J. H. You and K. Park, Design and additive manufacturing of thermal metamaterial with high thermal resistance and cooling capability, *Additive Manufacturing*, 41 (2021) 101947.

[15] X. T. Wang, B. Wang, X. W. Li and L. Ma, Mechanical properties of 3D re-entrant auxetic cellular structures, *International Journal of Mechanical Sciences*, 131 (2017) 396-407.

[16] H. Wang, Z. Lu, Z. Yang and X. Li, A novel re-entrant auxetic honeycomb with enhanced in-plane impact resistance, *Composite Structures*, 208 (2019) 758-770.

[17] N. K. Choudhry, B. Panda and S. Kumar, In-plane energy absorption characteristics of a modified re-entrant auxetic structure fabricated via 3D printing, *Composites Part B: Engineering*, 228 (2022) 109437.

[18] J. Zhang, G. Lu, D. Ruan and Z. Wang, Tensile behavior of an auxetic structure: analytical modeling and finite element analysis, *International Journal of Mechanical Sciences*, 136 (2018) 143-154.

[19] J. Zhang, G. Lu, Z. Wang, D. Ruan, A. Alomarah and Y. Durandet, Large deformation of an auxetic structure in tension: Experiments and finite element analysis, *Composite Structures*, 184 (2018) 92-101.

[20] J. Huang, Q. Zhang, F. Scarpa, Y. Liu and J. Leng, In-plane elasticity of a novel auxetic honeycomb design, *Composites Part B: Engineering*, 110 (2017) 72-82.

[21] S. I. Park and D. W. Rosen, Homogenization of mechanical properties for material extrusion periodic lattice structures considering joint stiffening effects, *Journal of Mechanical Design*, 140 (11) (2018) 111414.

[22] K. Bertoldi, V. Vitelli, J. Christensen and M. Van Hecke, Flexible mechanical metamaterials, *Nature Reviews Materials*, 2 (11) (2017) 1-11.

[23] T. Y. Kim, S. H. Park and K. Park, Development of functionally graded metamaterial using selective polymerization via digital light processing additive manufacturing, *Additive Manufacturing*, 47 (2021) 102254.

[24] Y. Kim, P. C. Nguyen, H. Kim, H. J. Choi and Y. Choi, Characterization and design of two-dimensional multi-morphology cellular structures for desired deformation, *Journal of Computational Design and Engineering*, 10 (2) (2023) 589-601.

[25] A. Fadeel, H. Abdulhadi, G. Newaz, R. Srinivasan and A. Mian, Computational investigation of the post-yielding behavior of 3D-printed polymer lattice structures, *Journal of Computational Design and Engineering*, 9 (1) (2022) 263-277.

Hong-Gap Choi is a M.Sc. candidate of the Department of Mechanical Design and Robot Engineering, Seoul National University of Science and Technology (SeoulTech), Seoul, Korea. He received his B.S in Mechanical System Design Engineering from SeoulTech. His research interests include additive manufacturing and automatic design.

Keun Park received his B.S. and M.Sc. degrees in Precision Engineering and Mechatronics from KAIST, Korea, in 1992 and 1994, respectively. He received his Ph.D. degree in Mechanical Engineering from KAIST in 1999. He is currently a Professor of the Department of Mechanical System Design Engineering at SeoulTech, Korea. His research interests are finite element analysis and optimization, additive manufacturing, and design for additive manufacturing (DfAM).